Density functional theory calculations of surface thermochemistry in Al/CuO thermite reaction

Hicham Jabraoui, Mehdi Djafari-Rouhani, Carole Rossi, Alain Esteve

To cite this version:

Hicham Jabraoui, Mehdi Djafari-Rouhani, Carole Rossi, Alain Esteve. Density functional theory calculations of surface thermochemistry in Al/CuO thermite reaction. Physical Review Materials, 2024, 8 (11), pp.115401. 10.1103/PhysRevMaterials.8.115401 . hal-04817899

HAL Id: hal-04817899
https://laas.hal.science/hal-04817899v1

Submitted on 4 Dec 2024

Density Functional Theory Calculations of Surface Thermochemistry in Al/CuO Thermite Reaction

Hicham Jabraoui,* Mehdi Djafari-Rouhani, Carole Rossi, and Alain Esteve†
LAAS-CNRS, University of Toulouse, CNRS, 7 avenue du Colonel Roche, 31400 Toulouse, France.

(Dated: December 4, 2024)

This paper investigates the thermochemistry of the heterogeneous Al/CuO thermite reaction through density functional theory calculations. We examine the interactions of atomic Al, Cu, O, as well as O_2, AlO, Al_2O, AlO_2, Al_2O_2 molecular species, with Al(111), Cu(111), and Al_2O_3 (γ and amorphous) surfaces, all of which being condensed phase products during the thermite reaction. Al(111) exhibits a very high reactivity, characterized by adsorption energies ranging from 3 to 5.3 eV for atomic Al, Cu, O, and from 4 to 9.5 eV for all molecular species. This reactivity is attributed to barrierless molecular decomposition, followed by the spatial spreading of adsorbate species across the surface facilitated by hot adatom migration processes. The Al_2O_3 surface also exhibits extremely high reactivity, with adsorption energies of 4.5 and 9.4 eV for atomic Cu and Al, respectively. Additionally, absorption energies range from 7 to 15 eV for condensation of Al_xO_y suboxides. Al-rich suboxides, namely Al_2O and Al_2O_2, show the greatest adsorption energy with -15.05 eV for Al_2O, against 6.52 eV for AlO_2. In contrast, O and O_2 exhibit no reactivity on Al_2O_3 surfaces exhibiting oxidation states being superior or equal to Al^{III}. Finally, Cu(111) surface exhibits much lower reactivity compared to Al(111) and Al_2O_3, with absorption energies ranging from 2 to 3.5 eV for Al, O and Cu atoms. Although energetic, molecular Al_xO_y suboxides show non dissociative adsorption on Cu(111). This findings point to different modes of oxide nucleation on these surfaces, pleading for planar nucleation and growth onto Al(111), while being more difficult and localised onto Cu(111). They renew our understanding of the thermite reaction chemistry, quantitatively differentiating the various type of heterogeneous reactions and their implication on the overall reaction. They also provide valuable data for higher-level diphasic simulations of the computational fluid dynamics, aiming to achieve predictive capability.

I. INTRODUCTION

Nanothermites are composed of nano-sized metal/metal oxide composites that can undergo redox reactions. They are promising energetic materials due to their high energy density and reactivity for energetic applications [1–5]. Aluminum (Al) stands out as the most extensively studied metallic fuel, owing to its high reaction enthalpy (84 $kJ.cm^{-3}$, 31 $kJ.g^{-1}$), widespread availability, cost-effectiveness and non-toxic nature. A variety of oxidizers have been studied, including copper oxide (CuO) [6, 7], iron oxide (Fe_2O_3)[8], molybdenum oxide (MoO_3)[9], tungsten oxide (WO_3)[10] and bismuth oxide (Bi_2O_3) [11]; the choice depending on the particular application. Applications of nanothermites include self-destructive devices [12, 13], semiconductor bridges [14–17] in order to initiate explosives, pyro-fuze [18, 19], welding repairs [20, 21]. On the fundamental science side, with the goal to investigate the complexity of thermite combustion, research has been conducted at different length scales. At the nanoscale, density functional theory (DFT) calculations [22], molecular dynamics (MD) simulations [23–25] and transmission electron microscopy (TEM) [26–28] have been used to depict major condensed phase reaction mechanisms. Results have highlighted the correlation between oxygen release (from oxidizer decomposition) and nanothermite ignition and provided very useful insights into the key role of reactive interfaces on the ignition threshold as observed experimentally [29–31]. On the other hand, micro-scale combustion behaviors have been actively investigated in the last decade using high-speed microscopy/thermometry [32]. Research has unravelled reactive sintering mechanisms [33] in Al-based nanothermite and highighted the key role of spatial heat transfer mechanisms occurring at the reaction front, which can be affected by impurities [34] or porosity [35]. Macroscopically, only a few theoretical studies [36–38] have attempted to explicitly account for the vapor-phase aluminum particles combustion in O_2 (released by the oxidizer decomposition), with results suggesting occurrence of the reactions over a broad pressure range of about 1 - 100 atm. They show that, as aluminum and alumina decompose, reaching their vaporization temperature, gaseous sub-oxides (Al_xO_y, where x=1,2 and y=1,2) are formed. This results in unsteady combustion within the gas phase, involving eight reactions [36–38], as well as heterogeneous reactions occurring at particle surfaces. For these heterogeneous reactions, a counting procedure incorporating 10 potential reactions was implemented instead of employing a detailed and rigorous chemical kinetics scheme [36–38].

However, in practice, Al combustion shows contrasted characteristics, notably highlighted by its burn rate dependency with particle diameter : burn rate follows a $d^{0.3}$ law compared to d^2 for micron size Al particle in air, d representing the Al particle diameter [39]. This raises

---

* hicham.jabraoui@gmail.com
† aesteve@laas.fr

fundamental questions on the influence of heterogeneous chemical reactions taking place at the fuel, and alumina (byproduct) surfaces following Al vaporization. Things become even more complex when Al burns in contact with a metallic oxidizer such as CuO in nanothermite materials. Key question are : where and how does alumina preferentially nucleate and grow, on Al or reduced metallic oxidizer ? Said differently: does the gaseous suboxides condense on both aluminum and reduced metallic oxidizer particles? Answering this is crucial for comprehending nanothermite burning behaviors and for developing predictive combustion models.

In this study, the interaction between each gaseous species *e.g.*, Al, Cu, O, O_2, Al_2O, Al_2O_2, AlO, AlO_2 with pure Al, Cu, and Al_2O_3 surfaces are theoretically investigated by DFT. The condensed phases are restricted to pure Al, Cu, and Al_2O_3 as we consider the combustion at the steady-state regime, thus above 2800 K, for which CuO is fully decomposed. DFT calculations are systematically conducted to determine adsorption energies and screen all surface sites of interest. This enables the establishment of a hierarchy of chemical processes on the various surfaces, thus facilitating the development of potential mechanistic scenarios for the thermite reaction.

II. COMPUTATIONAL AND MODEL DETAILS

DFT calculations were carried out using the Vienna *ab initio* Simulation Package (VASP)[40]. The calculations utilized the PBE density functional and the projector augmented wave (PAW) method, employing a plane-wave cutoff energy set at 400 eV. Due to the system's inherent antiferromagnetic ground state for Cu or CuO, spin-polarized calculations were conducted. Atomic positions were relaxed until the forces per atom reached values below 0.02 eV/Å. The self-consistent solution of the Kohn-Sham (KS) equations persisted until the energy difference between cycles fell below 10^{-6} eV [41–44]. Brillouin zone sampling was confined to the Γ point. To account for van der Waals interactions, the semiempirical D2 approach developed by Grimme was applied [45]. This level of theory has demonstrated success in prior studies concerning the adsorption of oxidizing molecular species, such as O_2 on mineral surfaces [22, 44, 46, 47]. All along the paper, we define the adsorption energy ΔE_{ads}, for the various species (respectively molecular and atomic) in interaction with the surfaces as:

$$\Delta E_{\text{ads}} = E(\text{surface+molecule}) - [E(\text{surface}) + E(\text{molecule})] \quad (1)$$

and

$$\Delta E_{\text{ads}} = E(\text{surface+atom}) - [E(\text{surface}) + E(\text{atom})] \quad (2)$$

Note that for atomic oxygen, the reference E(atom) becomes $1/2E(O_2)$. E(surface) represents the energy of the pristine Al(111), Cu(111), $Al_2O_3(100)$, or alumina (amorphous) surface. Similarly, E(molecule) and E(atom) represent the energy of isolated molecular and atomic species under consideration for adsorption, respectively. The adsorption can be either non-dissociative (an activation energy is necessary for dissociation) or dissociative without any activation. Al adsorption configuration convergence was checked through vibrational analysis. Note that the spin state for the reference ground states of the molecular species under consideration was determined: as a triplet state for molecular oxygen, doublet state for AlO, and singlet states for both Al_2O and Al_2O_2, while AlO_2 was showing partial filling of the two highest molecular orbitals. In addition, the thermodynamic stability of all gas phase species, as referred to as $1/2O_2$, Cu and Al chemical potential references are provided in Table I We also considered a separation energy ΔE_{sep}, which refers to as the difference in energy between the local adsorbate (disscosiated or not) and a configuration where all species of the molecular adsorbate are separated from each other as isolated adatoms. This separation energy allows indicating if the molecular species subunits thermodynamically prefer to be spread away from each other following local dissociation. Obviously, this separation is an activated process which might involve multiple activation barriers. The quantification of the kinetics of this separation is out of the scope of this article.

To account for the effect of temperature on the adsorption energy, the enthalpies ΔH_{ads} are defined as follows:

$$\Delta H_{\text{ads}} = H(\text{surface} + \text{atom}) - [H(\text{surface}) + E(\text{atom})] \quad (3)$$

Each enthalpy term, for each system species, is calculated by summing the electronic energy with contributions from vibrational, translational, and rotational partition functions:

$$H^i = H^i_0 + \text{ZPVE} + H^i_{\text{vib}} + H^i_{\text{trans}} + H^i_{\text{rot}} \quad (4)$$

where:

- H^i_0 is the formation enthalpy at 0 K.
- **ZPVE** (Zero-Point Vibrational Energy) is given by:

$$\text{ZPVE} = R \sum_i \left(\frac{h\nu_i}{2k} \right) \quad (5)$$

- $\boldsymbol{H_{\text{vib}}}$ (Vibrational Enthalpy) accounts for vibrational energy contributions at a given temperature:

$$H_{\text{vib}} = \left(\frac{R}{k} \right) \sum_i \left(\frac{h\nu_i}{\exp\left(\frac{h\nu_i}{kT}\right) - 1} \right) \quad (6)$$

- $\boldsymbol{H_{\mathbf{trans}}}$ (Translational Enthalpy) is:

$$H_{\mathrm{trans}} = \frac{5}{2}RT \tag{7}$$

- $\boldsymbol{H_{\mathbf{rot}}}$ (Rotational Enthalpy) is:

$$H_{\mathrm{rot}} = \begin{cases} \frac{3}{2}RT & \text{for non-linear molecules} \\ RT & \text{for linear molecules} \end{cases} \tag{8}$$

At a given temperature, the total enthalpy change upon adsorption becomes:

$$\begin{aligned} \Delta H_{\mathrm{ads}}(T) = \Delta E\,(0\,\mathrm{K}) + \Delta \mathrm{ZPVE} + \Delta H_{\mathrm{vib}} \\ + \Delta H_{\mathrm{rot}} + \Delta H_{\mathrm{trans}} \end{aligned} \tag{9}$$

Detailed expressions are as follows:

$$\Delta \mathrm{ZPVE} = R\sum_i \left(\frac{h\nu_i}{2k}\right) - R\sum_j \left(\frac{h\nu_j}{2k}\right) \tag{10}$$

$$\begin{aligned} \Delta H_{\mathrm{vib}} = \left(\frac{R}{k}\right)\sum_i \left(\frac{h\nu_i}{\exp\left(\frac{h\nu_i}{kT}\right) - 1}\right) \\ - \left(\frac{R}{k}\right)\sum_j \left(\frac{h\nu_j}{\exp\left(\frac{h\nu_j}{kT}\right) - 1}\right) \end{aligned} \tag{11}$$

$$\Delta H_{\mathrm{trans}} = -\frac{5}{2}RT \tag{12}$$

$$\Delta H_{\mathrm{rot}} = \begin{cases} -\frac{3}{2}RT & \text{for non-linear molecules} \\ -RT & \text{for linear molecules} \end{cases} \tag{13}$$

The summation over i refers to all vibrations of the surface-adsorbate system, representing the final state post-adsorption, while the summation over j includes the vibrational frequencies of the isolated surface and molecule (ν_i and ν_j frequencies, respectively). h is the Planck constant, k is the Boltzmann constant, and R is the gas constant. The developed code for this approach is available at this link: `https://github.com/JABRAOUI/Thermodynamic_corrections_adsorption_energy`[48]. Please cite the publication and code for further use.

We have chosen to calculate adsorption values at 2900 K, which is representative of the combustion process and is situated around the vaporization temperatures of both Al and Cu phases. This temperature facilitates the production of the considered gas-phase species as well as the presence of Al and Cu condensed phases. It is important to note that the melting temperatures of Al and Cu are 932 K and 1356 K, respectively, while their vaporization temperatures are 2600 K and 2868 K, respectively [49]. To illustrate the effect of temperature on adsorption, we calculated the adsorption free energy, expressed as:

$$\Delta G_{\mathrm{ads}} = \Delta H_{\mathrm{ads}} - T\Delta S_{\mathrm{ads}} \tag{14}$$

The calculation of free energy involves incorporating the change in entropy due to adsorption along with the enthalpy. To simplify the calculation of entropy, we utilized an empirical equation proposed by Campbell and Sellers [50]. After collecting data from equilibrium adsorption experiments and temperature-programmed desorption of alkanes and other small molecules from mineral and metal surfaces, they determined that the entropy of a molecule adsorbed on a surface retains most of its gas-phase entropy. This retention occurs because the molecule is trapped in a potential well, which is steep in the direction perpendicular to the surface, thereby restricting motion in that direction. They proposed the following empirical formula:

$$S_{\mathrm{ads}}(T) = 0.70 S_{\mathrm{gas}}(T) - 3.3R \tag{15}$$

Where:

- $S_{\mathrm{ads}}(T)$ is the entropy of the molecule in the adsorbed state.
- $S_{\mathrm{gas}}(T)$ is the entropy of the molecule in the gas phase.
- R is the universal gas constant.

Using the empirical formula, the change in entropy due to adsorption can be calculated as follows:

$$\Delta S_{\mathrm{ads}}(T) = S_{\mathrm{ads}}(T) - S_{\mathrm{gas}}(T) \tag{16}$$

Substituting the empirical relation yields:

$$\Delta S_{\mathrm{ads}}(T) = -0.30 S_{\mathrm{gas}}(T) - 3.3R \tag{17}$$

Finally, the equation to calculate the adsorption free energy is as follows:

$$\Delta G_{\mathrm{ads}} = \Delta H_{\mathrm{ads}}(T) + 0.30T \times S_{\mathrm{gas}}(T) + 3.3R \times T \tag{18}$$

This indicates that the molecule loses approximately 30% of its gas-phase entropy upon adsorption, along with a constant entropic loss of $3.3R$. The entropy S_{gas} is obtained from the NIST-JANAF Thermochemical Tables [51].

The charge density difference ($\Delta\rho$) and Bader charge difference (ΔQ) [52–54] was determined to enhance our understanding of the interaction between aluminum suboxide species and pure, Al(111)-, Cu(111)-, or Al_2O_3 surfaces. To visualize charge density modifications ($\Delta\rho$)

(utilizing VESTA [55]), we combined three charge densities: the density of the surface complex $\rho_{\text{surface-gas}}$, the density of the clean surface ρ_{surface}, and the density of the isolated molecule in vacuum ρ_{gas}, as depicted in the equation below [47]:

$$\Delta\rho = \rho_{\text{surface-gas}} - \rho_{\text{surface}} - \rho_{\text{gas}} \tag{19}$$

To obtain the difference in Bader charge ΔQ, the following equation was employed:

$$\Delta Q = Q_{\text{surface-gas}} - Q_{\text{surface\&gas}} \tag{20}$$

where $Q_{\text{surface-gas}}$ represents the Bader charge of all atoms upon adsorption, and $Q_{\text{surface\&gas}}$ is the Bader charge of the separated clean surface and the isolated molecule in the gaseous phase. Crystalline Al(111) and Cu(111) surfaces were constructed from the face-centered cubic (*fcc*) bulk arrangement using a primitive unit cell of dimensions $a = b = c = 4.05$ and 3.62 Å , $\alpha = \beta = \gamma = 90°$, respectively [56]. It has to be noted that the (111) surfaces were chosen for their stability and because they are well-documented model-surfaces both experimentally and theoretically [56, 57]. Respectively, associated super-cells of dimensions $9.92 \times 8.59 \times 35$ Å and $7.60 \times 8.77 \times 35$ Å were generated (Figures 1). Note that, to create the surfaces, we introduced a vacuum space in the direction normal to the surface, of roughly 25 Å at the cleavage plane, *i.e.*, the net distance separating the bottom and surface slab monolayers across the vacuum. Both super-cells surfaces were composed of 72 atoms, 6 layers of 12 atoms by layer, thus respecting the ABC stacking symmetry of the fcc lattice in the [111] direction. The two bottom layers were kept fixed during minimization in a manner to mimic a real bulk constrain. These surfaces exhibit three high-symmetry surface sites for adsorption: *fcc*, hexagonal close-packed (*hcp*), and top sites (*top*), as well as bridge position (*bridge*), as pictured in Figure 1. From our calculations, we here report results at *fcc*, *hcp*, and *top* sites, as the *bridge* site was found to be unstable upon relaxation in the adsorption calculations. We will only consider single molecular adsorptions within the cell surface. Given the lateral cell dimension, and counting 12 fcc or hcp sites, we can consider that a coverage of of nearly 8% is achieved for atomic species.

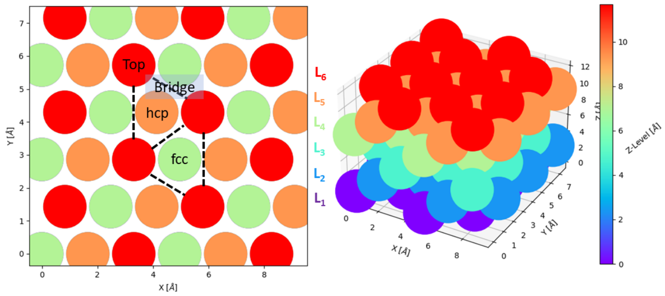

FIG. 1: 3D (right side) and top (left side) views of the *fcc*, *hcp*, *top*, and *bridge* sites for adsorption on Al(111), which are also applicable to Cu(111).

A crystalline Al_2O_3 surface was crafted, adopting a cubic arrangement derived from a primitive unit-cell with dimensions $a = b = c = 8.88$ Å and angles $\alpha = \beta = \gamma = 90°$. This structured surface aligns with the Ia3^{-} space group [58]. The (100) surface illustrated in Figure 2, was generated by extending the unit-cell to 17.75×17.75 (lateral dimensions) $\times$ 40 Å (a vacuum space of 31 Å was added in the direction perpendicular to the cleavage plane). This super-cell is composed of 128 Al atoms and 192 O atoms. Together with a crystalline aluminum oxide model surface, presenting a restricted number of adsorption sites, including Al^{IV} and Al^{V} oxidation states for aluminum atoms exposed to the gas phase, we also generated an amorphous surface. Again only single species are adsorbed on this model surface, which corresponds to similar coverages as for the metal surfaces, roughly 10%. The amorphous surface is chemically closer to the real system being in a liquid state. This allows studying deviation from the crystalline surface and brings additional surface configurations, such as lower oxidation states for surface aluminum atoms (such as Al^{III}). As a first step, a bulk of amorphous Al_2O_3 was built from classical MD simulations using the melting-quenching method by Jabraoui and co-workers [59–63]. Additional details can be found in the Supplemental Material ([64, 65], See Supplemental Material) file. The Al_2O_3 glassy state consisting of 92 Al and 138 O from classical MD simulations underwent a DFT relaxation and was subsequently cleaved in a plane perpendicular to the z direction, forming a new box for the alumina surface with dimensions of 17.75 Å × 17.75 Å × 28.5 Å. To facilitate further relaxation, a void of 20 Å was introduced at the cleavage plane, representing the net distance separating the bottom and surface slab monolayers across the vacuum. For any considered surface, to mitigate polar effects, linear dipole corrections were applied, following their implementation in VASP. The two bottom monolayers were held frozen to emulate bulk constraints.

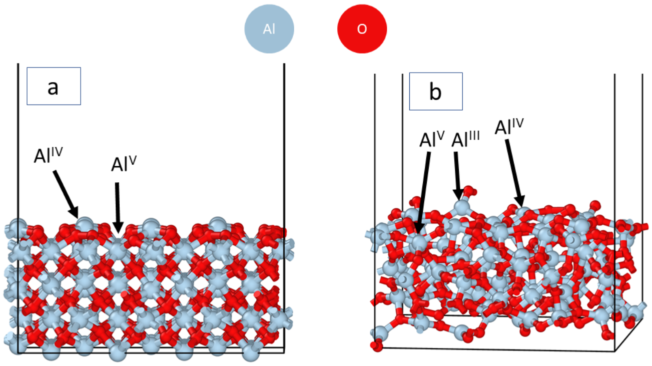

FIG. 2: (a) γ-Al_2O_3 and (b) amAl_2O_3. Steel blue balls represent Al atoms and red balls represent O atoms. For adsorption calculations, we considered exposed oxygen and units of Al, specifically Al^{IV} or Al^{V} for the crystalline surface of $Al_2O_3(100)$, and Al^{III}, Al^{IV}, or Al^{V} for the amAl_2O_3.

We considered 8 gaseous species : Al, Cu, O, O_2, Al_2O, Al_2O_2, AlO and AlO_2, which are present during the Al/CuO reaction. Equilibrium bond lengths and angles of O_2 and Al suboxides (Al_xO_y) molecules considered isolated are detailed in Table I

III. RESULTS

A. Comparative adsorption of Cu, Al, O atoms and O_2, AlO, Al_2O, AlO_2, Al_2O_2 molecules on Cu(111) and Al(111) surfaces

The adsorption energies (ΔE_{ads}) of the different gaseous species onto Al(111) and Cu(111) are presented in Table II and Figure 3. When available, data from the literature are added for comparison purpose. The interatomic distance between the adsorbed atomic and molecular species and the surface are given in Table III. The Bader charge difference (ΔQ_{atomic}) upon adsorption of the different aluminum molecular suboxides are summarized in Table IV. The subscript 'Sp' refers to as atoms belonging to the adsorbed species (molecular or atomic), whereas the subscript 'S' refers to as the surface atoms. And finally, Figure 4 gives a visualization of the most stable adsorbed configurations onto Cu(111) and Al(111) surfaces.

Starting with O on Cu(111) and Al(111), the *fcc* configuration emerges as the most stable, with an energy gain of 2.10 and 5.27 eV upon adsorption, respectively. The Al(111) surface exhibits a significantly higher affinity for O compared to the Cu(111) surface, with an energy difference of approximately 3 eV. The O-Cu and O-Al distances are in the range of 1.90-1.91 Å and 1.84-1.96 Å , respectively.

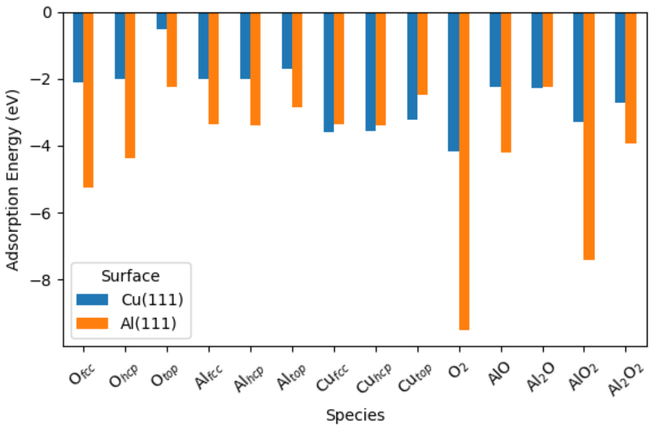

FIG. 3: Histograms comparing the adsorption energies (ΔE_{ads} in eV) on Cu(111) and Al(111) surfaces for various species, namely O, Al, and Cu atoms, O_2, AlO, Al_2O, AlO_2, and Al_2O_2 molecules.

Considering Al atoms, both *fcc* and *hcp* configurations are stable on the Cu(111), exhibiting similar energy gain of roughly $\sim$ 2 eV. The Al-Cu distance is measured at 2.32-2.37 Å. The Al(111) surface shows higher reactivity with Al atoms, with an adsorption energy of roughly -3.4 eV for both *fcc* and *hcp* sites.

As for Al atoms, *fcc* and *hcp* Cu adsorption configurations are the most stable on both surfaces. Onto Cu(111), the energy gain is of $\sim$ 3.59 eV. The Cu-Cu distance is calculated at 2.36-2.38 Å. On Al(111), the *hcp* configuration is slightly more stable with a gain of 3.38 eV. The Cu-Al distance is of 2.38-2.40 Å. Interestingly, the adsorption of Cu atoms is rather similar on both Al(111) and Cu(111) surfaces with a slight energy difference of approximately 0.11 eV, which contrasts with the preceding case of the hierarchical adsorption of the aluminum atom.

Considering O_2 molecules, Cu(111) is characterized by a strong and dissociative -4.16 eV adsorption and an associated Cu-O interatomic distances in the range 1.82–1.90 Å. Al(111) presents an even more favorable scenario, with a dissociative adsorption energy of -9.51 eV (1.86–1.88 Åbond length range). Interestingly, surface separating of oxygen adatoms allows gaining another $\Delta E_{\text{sep}} = 1$ eV for the reaction (2×-5.27 eV adsorption to be compared with 9.51 eV local dissociative adsorption). It is worth noting that, experimentally, Brune et al.[71] identified systematic oxygen separation following dissociation at room temperature (via Scanning Tunneling Microscopy imaging). They argued that the amount of chemical energy gained upon dissociation would make it possible to activate further surface migration, spatially separating adatoms; they introduced the notion of "hot adatom migration". Along this line, examination of Bader charge distribution, showing a net charge of -1.7 e on both adsorbed oxygen atoms, is one explanation of the extra energy loss in clustering surface oxygen atoms

TABLE I: Geometries and formation energies (in eV)

of adsorbed gaseous O_2 and Al$_x$O$_y$ molecules on surfaces. 'Sp' refers to the species atoms, and 'S' refers to the surface atoms. The geometrical parameters include bond lengths ($Al_{Sp} - Al_{Sp}$, $Al_{Sp} - O_{Sp}$, $O_{Sp} - O_{Sp}$) (in Å) and bond angles ($\theta_{O_{Sp}-Al_{Sp}-O_{Sp}}$, $\theta_{Al_{Sp}-O_{Sp}-Al_{Sp}}$) in degrees (°).

Species	$Al_{Sp} - Al_{Sp}$ (Å)	$Al_{Sp} - O_{Sp}$ (Å)	$O_{Sp} - O_{Sp}$ (Å)	$\theta_{O_{Sp}-Al_{Sp}-O_{Sp}}$ (°)	$\theta_{Al_{Sp}-O_{Sp}-Al_{Sp}}$ (°)	Formation Energy (eV)
Cu	–	–	–	–	–	-0.23
Al	–	–	–	–	–	-0.09
O_2	–	–	1.24	–	–	-8.85
AlO	–	1.63	–	–	–	-7.67
Al_2O	3.31	1.91	–	–	120	-13.58
AlO_2	–	1.67	3.33	180	–	-14.13
Al_2O_2	2.41	1.76	2.57	94	87	-20.86

TABLE II: Adsorption energies (ΔE_{ads} in eV) for the different gaseous species on Cu(111) and Al(111) surfaces. For the gaseous Al$_x$O$_y$, only the adsorption energies corresponding to the most stable configurations are given.

Species	**Config.**	$\mathbf{\Delta E_{ads}}$ **(eV)**									
		Cu(111)					**Al(111)**				
		0 K	300 K	2000 K	2900 K	Literature	0 K	300 K	2000 K	2900 K	Literature
O atom	*fcc*	-2.10	-2.09	-2.18	-2.22	-2.22[66]	-5.27	-4.32	-4.12	-3.83	-4.85[67], -4.90[68]
	hcp	-2.01	-2.00	-2.09	-2.13	-2.17[69]	-4.39	-4.37	-4.47	-4.51	-4.41[67]
	top	-0.54	-0.59	-0.95	-1.14		-2.25	-2.31	-2.83	-3.09	
Al atom	*fcc*	-2.02	-2.03	-2.10	-2.14		-3.37	-3.37	-3.45	-3.49	
	hcp	-2.00	-2.01	-2.08	-2.12		-3.38	-3.38	-3.46	-3.50	
	top	-1.71	-1.78	-2.13	-2.31		-2.84	-2.90	-3.26	-3.44	
Cu atom	*fcc*	-3.59	-3.60	-3.67	-3.71		-3.35	-3.37	-3.60	-3.71	
	hcp	-3.58	-3.59	-3.66	-3.70		-3.38	-3.38	-3.46	-3.50	
	top	-3.22	-3.28	-3.64	-3.82		-2.50	-2.56	-2.92	-3.10	
O_2		-4.16	-4.19	-4.25	-4.29	-4.47[69]	-9.51	-9.50	-9.43	-9.39	-8.80[70], -9.53[67], -10.21
AlO		-2.24	-2.24	-2.16	-2.12		-4.22	-4.22	-4.30	-4.34	
Al_2O		-2.29	-2.21	-1.79	-1.57		-2.26	-2.18	-1.76	-1.54	
AlO_2		-3.30	-3.23	-2.80	-2.58		-7.43	-7.35	-6.93	-6.71	
Al_2O_2		-2.71	-2.58	-1.88	-1.50		-3.94	-3.79	-3.10	-2.73	

locally. The coulombic repulsion is therefore one additional contribution in the direction of adsorbate spatial separation on the surface. Importantly, this coulombic repulsion contribution in much less operative onto the Cu(111) surface (-0.9 e charge on the atom), and no energy gain is calculated when separating both surface oxygen atoms.

Considering now aluminum suboxide species, AlO, Al_2O, AlO_2, Al_2O_2, adsorbed on Cu(111), the hierarchy of configurational stability is as follows:

1. AlO_2 exhibits the most stable configuration, with an energy of -3.30 eV. Interatomic distances include $Al_{\mathrm{Sp}} - Cu_{\mathrm{S}}$ (2.41-2.70 Å) and $O_{\mathrm{Sp}} - Cu_{\mathrm{S}}$ (2.00-2.11 Å). Bader charge calculation shows contributions from both aluminum (0.26 e) and oxygen (-0.17 -0.29 e). In the gas phase, AlO_2 exhibits a configuration characterized by a $O_{\mathrm{Sp}} - Al_{\mathrm{Sp}}$ bond distance of 1.67 Å and $\theta_{\text{O-Al-S}}$ angles of 180° (Table I). Upon adsorption, a slight bond stretching is observed with $O_{\mathrm{Sp}} - Al_{\mathrm{Sp}}$ distances in the range 1.76- 1.78 Å and $\theta_{O_{Sp}-Al_{Sp}-O_{Sp}}$ angle at approximately 116°. These structural modifications are not sufficient to postulate a full dissociative adsorption process that would require overcoming an activation energy.

2. Al_2O_2 follows with an energy of -2.71 eV and interatomic distances: $Al_{\mathrm{Sp}} - Cu_{\mathrm{S}}$ of 2.65-2.73 Åand $O_{\mathrm{Sp}} - Cu_{\mathrm{S}}$ of 2.20 Å. Bader charge differences reveal that aluminum (-0.30 -0.29 e) contributes more than oxygen (-0.03 -0.02 e) in the adsorption chemistry. In the gas phase, Al_2O_2 exhibits a configuration with $O_{\mathrm{Sp}} - Al_{\mathrm{Sp}}$ bond length of 1.76 Åand $\theta_{\text{O-Al-O}}$ angles at 94°, its stable state [72]. Upon adsorption, it experiences stretching with $O_{\mathrm{Sp}} - Al_{\mathrm{O}}$ distances around 1.8 Å and slight modification of the $\theta_{O_{Sp}-Al_{Sp}-O_{Sp}}$ angles, at approximately 90°. These value, as for the preceding case, plead for a non-dissociative adsorption process for Al_2O_2.

3. AlO similarly shows a non dissociative adsorp-

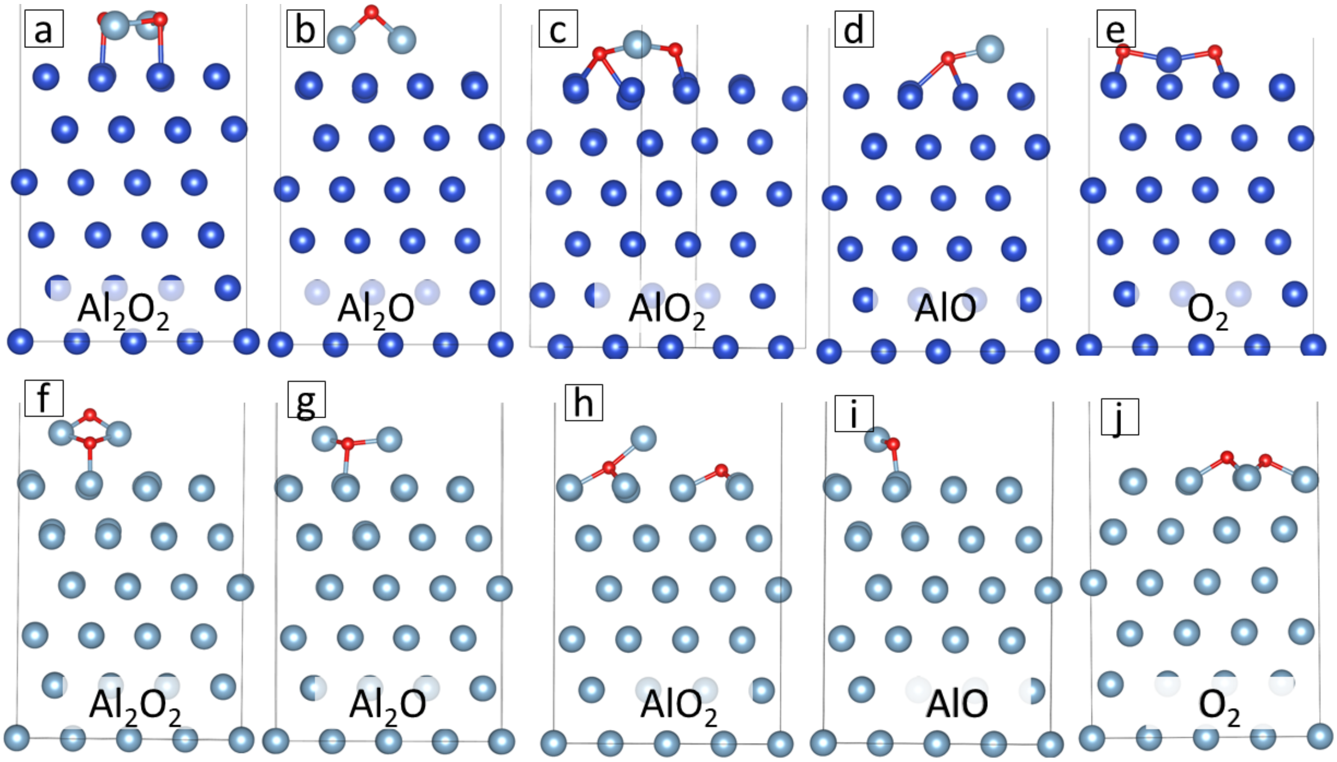

FIG. 4: Most stable configurations of adsorbed Al_2O_2, Al_2O, AlO_2, AlO, O_2 on Cu(111) surface (a–e) and Al(111) surface (f–j). Steel blue balls represent Al atoms, blue balls represent Cu atoms, and red balls represent O atoms.

tion energy of -2.29 eV, with interatomic distances: $Al_{\mathrm{Sp}}-Cu_{\mathrm{S}}$ (ranging from 2.57 to 2.35 Å), $O_{\mathrm{Sp}}-Cu_{\mathrm{S}}$ (2.18 Å), and $Al_{\mathrm{Sp}}-O_{\mathrm{Sp}}$ (1.73 Å). Bader charge analysis indicates contributions from both oxygen (0.12 e) and aluminum (-0.09 e). In the gas phase, AlO exhibits a configuration with a $O_{\mathrm{Sp}}-Al_{\mathrm{Sp}}$ bond distance of 1.63 Å. Upon adsorption, it undergoes stretching with $O_{\mathrm{Sp}}-Al_{\mathrm{S}}$ distances of 1.73 Å.

4. Finally, Al_2O presents also a non-dissociative adsorption energy of -2.26 eV, with interatomic distances: $Al_{\mathrm{Sp}}-Cu_{\mathrm{S}}$ (2.65-2.79 Å), $O_{\mathrm{Sp}}-Cu_{\mathrm{S}}$ (1.76 Å), and $Al_{\mathrm{Sp}}-O_{\mathrm{Sp}}$ (1.73 Å) (Table III). Bader charge differences reveal only aluminum (-0.71 -0.73 e) contributes to the adsorption, demonstrating the poor affinity of copper with oxygen. In the gas phase, Al_2O adopts a configuration with $O_{\mathrm{Sp}}-Al_{\mathrm{Sp}}$ bond distance at 1.91 Å and $\theta_{\text{Al-O-Al}}$ angles at 120° (Table I). Upon adsorption, it undergoes deformation, resulting in bond stretching with $O_{\mathrm{Sp}}-Al_{\mathrm{Sp}}$ distances of 1.7 Å and $\theta_{Al_{Sp}-O_{Sp}-Al_{Sp}}$ angles at approximately 116°.

On Cu(111) and for all aluminum suboxide species, the $Al_{\mathrm{Sp}}-O_{\mathrm{Sp}}$ distance upon adsorption remains similar to that of the alumina system [73], indicating that no dissociation is taking place during minimization, upon adsorption on the Cu(111) surface, as also seen from the adsorbed configurations shown in Figure 4. Overcoming some activation barrier (not calculated here) allows gaining a limited amount of energy. Indeed, estimating ΔE_{sep} for all configurations shows that a limited gain per atom (at around 1 eV) will be operated, that should not be so different from the gain in locally decomposing the adsorbed molecules, as for the O2 case discussed earlier.

TABLE IV: Bader charge difference (ΔQ_{atomic} in e) upon adsorption of the different aluminum suboxides on Al(111) and Cu(111) surfaces. 'Sp' refers to atoms from molecular species and 'S' refers to surface atoms.

	ΔQ_{atomic} (e) on Cu(111)		
Species	Al_{Sp}	O_{Sp}	Cu_{S}
AlO	-0.09	0.12	-0.10 − -0.20 & 0.32
Al_2O	-0.71 & -0.73	-0.08	0.16 − 0.35
AlO_2	0.26	0.17 − 0.29	0.31 & -0.14 − -0.25
Al_2O_2	-0.30 − -0.29	-0.03 − -0.02	0.49(2) & -0.08 − -0.09

	ΔQ_{atomic} (e) on Al(111)		
Species	Al_{Sp}	O_{Sp}	Al_{S}
AlO	-0.09	0.12	0.32 & -0.09 − -0.20
Al_2O	0.18 − 0.20	0.12	-0.62
AlO_2	1.43	0.63 − 0.93	-0.48 − -0.74
Al_2O_2	0.41 − 0.43	0.22	-0.19 − -0.67

TABLE III: Geometries of the adsorbed gaseous species onto Cu(111) and Al(111) surfaces, where 'Sp' refers to as Species and 'S' refers to as the Surface.

Species	**Distance Bond Lengths (Å) on Cu(111)**						**Distance Bond Lengths (Å) on Al(111)**					
	$Al_{Sp}-Cu_S$	$O_{Sp}-Cu_S$	$Al_{Sp}-O_{Sp}$	$O_{Sp}-O_{Sp}$	$Al_{Sp}-Al_{Sp}$	$Cu_{Sp}-Cu_S$	$Al_{Sp}-Al_S$	$O_{Sp}-Al_S$	$Al_{Sp}-O_{Sp}$	$O_{Sp}-O_{Sp}$	$Al_{Sp}-Al_{Sp}$	$Cu_{Sp}-Al_S$
O_{fcc}	−−	1.90-1.91	−−	−−	−−	−−	−−	1.84-1.96	−−	−−	−−	−−
O_{top}	−−	1.73	−−	−−	−−	−−	−−	1.69	−−	−−	−−	−−
O_{hpc}	−−	1.91	−−	−−	−−	−−	−−	1.88	−−	−−	−−	−−
Al_{fcc}	2.32-2.37	−−	−−	−−	−−	−−	2.63-2.78	−−	−−	−−	−−	−−
Al_{top}	2.19	−−	−−	−−	−−	−−	2.52	−−	−−	−−	−−	−−
Al_{hpc}	2.30-2.37	−−	−−	−−	−−	−−	2.61	−−	−−	−−	−−	−−
Cu_{fcc}	−−	−−	−−	−−	−−	2.36-2.38	−−	−−	−−	−−	−−	2.38-2.40
Cu_{top}	−−	−−	−−	−−	−−	2.22	−−	−−	−−	−−	−−	2.24
Cu_{hpc}	−−	−−	−−	−−	−−	2.38	−−	−−	−−	−−	−−	2.37
O_2	−−	1.82-1.90	−−	3.60	−−	−−	−−	1.86-1.88	−−	5.90	−−	−−
Al_2O	2.32-2.53	3.16	1.74	−−	2.68	−−	2.67-2.85	1.87	1.84	−−	3.28	−−
AlO	2.57-2.35	2.18	1.73	−−	−−	−−	2.65-2.79	1.76	1.73	−−	−−	−−
Al_2O_2	2.65-2.73	2.20	1.81	2.56	2.51	−−	2.60-3.08	1.82-4.51	1.87-1.76	2.54	2.54	−−
AlO_2	2.41-2.70	2.11-2.00	1.76-1.78	3.00	−−	−−	2.85-2.81	2.00-1.87	1.98,3.68	4.92	−−	−−

Species	**Angles (°) on Cu(111)**		**Angles (°) on Al(111)**	
	$\theta_{O_{Sp}-Al_{Sp}-O_{Sp}}$	$\theta_{Al_{Sp}-O_{Sp}-Al_{Sp}}$	$\theta_{O_{Sp}-Al_{Sp}-O_{Sp}}$	$\theta_{Al_{Sp}-O_{Sp}-Al_{Sp}}$
Al_2O	−−	116	−−	163
AlO_2	101	−−	118	−−
Al_2O_2	97 & 89	88 & 88	89 & 89	86 & 92

The following hierarchy on the adsorption of aluminum suboxides onto Al(111) is observed:

1. AlO_2 exhibits the highest adsorption stability with an energy of -7.43 eV and specific interatomic distances: $Al_{\mathrm{Sp}}-Al_{\mathrm{S}}$ (2.85-2.81 Å), $O_{\mathrm{Sp}}-Al_{\mathrm{S}}$ (2.00-1.87 Å), $Al_{\mathrm{Sp}}-O_{\mathrm{Sp}}$ (1.98 Å & 3.68 Å), and $O_{\mathrm{Sp}}-O_{\mathrm{Sp}}$ (4.92 Å). Bader charge analysis confirms aluminum (-0.71 and -0.73 e) as the primary contributor to adsorption. In the gas phase, AlO_2 has a configuration with $O_{\mathrm{Sp}}-Al_{\mathrm{Sp}}$ bond distance of 1.67 Å and $\theta_{\text{O-Al-S}}$ angles at 180° (Table I). Upon adsorption, it undergoes barrierless dissociation, resulting in $O_{\mathrm{Sp}}-Al_{\mathrm{Sp}}$ distances ranging around 1.98 Å & 3.68 Å and $\theta_{O_{SP}-Al_{Sp}-O_{Sp}}$ angles approximately at 163°. Despite of the observed molecular dissociation into AlO and O subunits and its high exothermicity, there is still ΔE_{sep} = -5.48 eV potential energy gain in completing the dissociation and spatial separation on the substrate.

2. Next is AlO with an energy of -4.22 eV and interatomic distances: $Al_{\mathrm{Sp}}-Al_{\mathrm{S}}$ (2.65-2.79 Å), $O_{\mathrm{Sp}}-Al_{\mathrm{S}}$ (1.76 Å), $Al_{\mathrm{Sp}}-O_{\mathrm{Sp}}$ (1.73 Å). Bader charge differences show contributions from both oxygen (0.12 e) and aluminum (-0.09 e), with slightly higher oxygen contribution. In the gas phase, AlO exhibits a configuration with $O_{\mathrm{Sp}}-Al_{\mathrm{Sp}}$ bond distance of 1.63 Å. Upon adsorption, it undergoes expansion without dissociation, with $O_{\mathrm{Sp}}-Al_{\mathrm{S}}$ distances around 1.73 Å. Despite the considerable chemisorption energy showing partial dissociation, as in the preceding case another ΔE_{sep} = -4.42 eV can be gained upon further dissociation and surface separation,

3. Al_2O_2 demonstrates an energy of -3.94 eV, with corresponding interatomic distances: $Al_{\mathrm{Sp}}-Al_{\mathrm{S}}$ (2.60-3.08 Å), $O_{\mathrm{Sp}}-Al_{\mathrm{S}}$ (1.82-4.51 Å), $Al_{\mathrm{Sp}}-O_{\mathrm{Sp}}$ (1.76-1.87 Å), and $O_{\mathrm{Sp}}-O_{\mathrm{Sp}}$ (2.54 Å). Bader charge differences emphasize aluminum's contribution (0.41 & 0.43 e), exceeding that of oxygen (-0.22 e). In the gas phase, the configuration of Al_2O_2 is characterized by $O_{\mathrm{Sp}}-Al_{\mathrm{Sp}}$ bond distance at 1.77 Å , and both $\theta_{\text{O-Al-S}}$ angles at 93.5°, recognized as the most stable configuration[72]. Upon adsorption, it undergoes deformation without complete dissociation, with $O_{\mathrm{Sp}}-Al_{\mathrm{Sp}}$ ranging be-

tween 1.76-1.87 Å and $\theta_{O_{Sp}-Al_{Sp}-O_{Sp}}$ angles at 70.7 & 71.1°. In this specific case, a huge chemical energy is stored in this metastable configuration as ΔE_{sep} = -13.34 eV can be gained for fully decomposing the adsorbate, demonstrating its role as an intermediate surface state.

4. Finally, Al_2O has an energy of -2.26 eV and interatomic distances: $Al_{\text{Sp}} - Al_{\text{S}}$ (2.67-2.85 Å), $O_{\text{Sp}} - Al_{\text{S}}$ (1.87 Å), $Al_{\text{Sp}} - O_{\text{Sp}}$ (1.84 Å). Bader charge differences reveal aluminum (1.43 e) contributes more than oxygen (0.63 & 0.93 e). In the gaseous phase, Al_2O adopts a configuration with $O_{\text{Sp}} - Al_{\text{Sp}}$ bond distance measures 1.91 Å, and both $\theta_{\text{Al-O-Al}}$ angles equal 120°, as outlined in Table I, while upon adsorption, it experiences deformation without dissociation, resulting in the stretxhing of $O_{\text{Sp}} - Al_{\text{Sp}}$ distances, measuring 1.84 Å, and $\theta_{Al_{Sp}-O_{Sp}-Al_{Sp}}$ angles at approximately 163°. The observation is similar to that of Al_2O_2, with here an amount of energy gain of ΔE_{sep} = -0.75 eV in fully decomposing and separating surface species.

Overviewing these hierarchies, AlO_2 exhibits the highest stability on both Al(111) and Cu(111) surfaces, due to the reactivity of the two single-bonded oxygen atoms. This is particularly evident for the aluminum surface, where the system converges towards two bridging oxygen configurations. Additionally, the aluminum surface systematically exhibits higher adsorption energies and a propensity to distort, if not directly dissociate, the aluminum suboxides. In contrast, the consistent $Al_{\text{Sp}} - O_{\text{Sp}}$ distances on Cu(111) indicate the higher stability of the non-dissociated configuration, emphasizing the robustness of the aluminum-oxygen bond on Cu(111) and the differing chemistries of these surfaces during the thermite reaction.

Table II presents the adsorption energies (ΔE_{ads}) for various gaseous species on Cu(111) and Al(111) surfaces at different temperatures (0 K, 300 K, 2000 K, and 2900 K). Analyzing these data allows us to draw several conclusions about the temperature dependence of adsorption energies for these species.

For the O atom on the Cu(111) surface, the adsorption energy increases slightly with increasing temperature, ranging from -2.10 eV at 0 K to -2.22 eV at 2900 K at the fcc site. Similarly, on the Al(111) surface, the adsorption energy decreases from -5.27 eV at 0 K to -3.83 eV at 2900 K at the fcc site. This indicates that the strength of oxygen adsorption weakens as the temperature rises on Al(111), but remains relatively stable on Cu(111).

For the Al atom, the adsorption energy on the Cu(111) surface increases slightly from -2.02 eV at 0 K to -2.14 eV at 2900 K at the fcc site. On the Al(111) surface, the adsorption energy decreases from -3.37 eV at 0 K to -3.49 eV at 2900 K at the fcc site. This suggests that aluminum atoms experience weaker adsorption on Al(111) with increasing temperature, whereas the adsorption on Cu(111) remains relatively strong.

The adsorption energy of the Cu atom on the Cu(111) surface shows a slight increase with temperature, ranging from -3.59 eV at 0 K to -3.71 eV at 2900 K at the fcc site. On the Al(111) surface, the adsorption energy also shows a slight increase from -3.35 eV at 0 K to -3.71 eV at 2900 K at the fcc site, indicating stable adsorption on both surfaces across the temperature range.

Furthermore, when comparing different configurations of O, Al, and Cu on both surfaces, the stability of the adsorption sites (fcc, hcp, and top) can vary with temperature. For the O atom, the fcc site is generally the most stable on both surfaces at lower temperatures, characterized by the highest adsorption energies. As temperature increases, the stability of the fcc site slightly decreases, making the hcp site more competitive, especially on Al(111). The Al atom shows similar trends, where the fcc site typically remains the most stable, but the difference between fcc and hcp sites diminishes with increasing temperature. On Cu(111), the top site becomes significantly less stable as temperature rises, as indicated by the lower adsorption energies, a trend also observed for Cu atoms. The high-temperature behavior suggests that at elevated temperatures, the relative stability of these sites can shift, leading to changes in adsorption preferences, but overall, the fcc and hcp sites remain the most stable compared to the top site, consistent with the stronger adsorption interactions at these sites.

For the oxygen molecule (O_2), the adsorption energy on the Cu(111) surface increases slightly with temperature, from -4.16 eV at 0 K to -4.29 eV at 2900 K. Conversely, on the Al(111) surface, the adsorption energy decreases from -9.51 eV at 0 K to -9.39 eV at 2900 K. This indicates a slight increase in adsorption strength on Cu(111) but a decrease on Al(111) with rising temperature.

The adsorption energy of AlO on the Cu(111) surface decreases slightly from -2.24 eV at 0 K to -2.12 eV at 2900 K. On the Al(111) surface, the adsorption energy increases with temperature, from -4.22 eV at 0 K to -4.34 eV at 2900 K, suggesting stronger adsorption on Al(111) at higher temperatures.

For Al_2O, the adsorption energy on the Cu(111) surface decreases from -2.29 eV at 0 K to -1.57 eV at 2900 K. A similar decrease is observed on the Al(111) surface, from -2.26 eV at 0 K to -1.54 eV at 2900 K, indicating weaker adsorption with rising temperature on both surfaces.

The adsorption energy of AlO_2 on the Cu(111) surface remains relatively stable across the temperature range, from -3.30 eV at 0 K to -2.58 eV at 2900 K. On the Al(111) surface, the adsorption energy also remains stable, from -7.43 eV at 0 K to -6.71 eV at 2900 K, indicating consistent adsorption behavior with temperature for AlO_2.

The adsorption energy of Al_2O_2 on the Cu(111) surface

TABLE V: Adsorption free energies (ΔG_{ads} in eV) for different gaseous species on Cu(111) and Al(111) surfaces. Adsorption energies are given for the most stable configurations of gaseous Al_xO_y.

Species	**Config.**	**Cu(111)**				**Al(111)**			
		0 K	**300 K**	**2000 K**	**2900 K**	**0 K**	**300 K**	**2000 K**	**2900 K**
O atom	*fcc*	-2.10	-1.85	-0.61	0.06	-5.27	-5.02	-3.78	-3.11
	hcp	-2.01	-1.77	-0.52	0.15	-4.39	-4.14	-2.90	-2.23
	top	-0.54	-0.35	0.62	1.14	-2.25	-2.07	-1.26	-0.81
Al atom	*fcc*	-2.02	-1.80	-0.51	0.17	-3.37	-3.13	-1.86	-1.18
	hcp	-2.00	-1.78	-0.49	0.19	-3.38	-3.14	-1.87	-1.19
	top	-1.71	-1.54	-0.53	-0.01	-2.84	-2.66	-1.66	-1.08
Cu atom	*fcc*	-3.59	-3.36	-2.07	-1.39	-3.35	-3.13	-1.99	-1.39
	hcp	-3.58	-3.35	-2.06	-1.38	-3.38	-3.14	-1.86	-1.17
	top	-3.22	-3.04	-2.03	-1.50	-2.50	-2.32	-1.31	-0.78
O_2		-4.16	-3.91	-2.41	-1.61	-9.51	-9.23	-7.59	-6.72
AlO		-2.24	-1.95	-0.23	0.67	-4.22	-3.93	-2.38	-1.55
Al_2O		-2.29	-1.89	0.35	1.53	-2.26	-1.86	0.38	1.56
AlO_2		-3.30	-2.91	-0.67	0.52	-7.43	-7.03	-4.80	-3.61
Al_2O_2		-2.71	-2.23	0.44	1.85	-3.94	-3.44	-0.79	0.63

decreases from -2.71 eV at 0 K to -1.50 eV at 2900 K. On the Al(111) surface, the adsorption energy decreases from -3.94 eV at 0 K to -2.73 eV at 2900 K, indicating weaker adsorption with increasing temperature on both surfaces.

Taking into account the entropy contributions in the adsorption of the considered species on both surfaces, Table V and Figure 5 present the adsorption free energies (ΔG_{ads}) for various gaseous species on Cu(111) and Al(111) surfaces at different temperatures (0 K, 300 K, 2000 K, and 2900 K). Analyzing these data reveals the temperature dependence of adsorption energies for these species.

For the O atom on the Cu(111) surface, the adsorption free energy is drastically decreased (absolute value) with temperature, shifting to a slightly positive value, from -2.10 eV at 0 K to 0.06 eV at 2900 K, indicating that the adsorption becomes unlikely at the fcc site. On the Al(111) surface, the adsorption free energy also decreases, but still remains significative from -5.27 eV at 0 K to -3.11 eV at 2900 K at the fcc site.

The same behaviour is obtained for the Al atom, the adsorption free energy on the Cu(111) surface becomes positive at 2900K (0.17 eV, on the fcc site). while decreasing from -3.37 eV at 0 K to -1.18 eV at 2900 K on the Al(111) fcc site.

The adsorption free energy of the Cu atom on the Cu(111) surface increases from -3.59 eV at 0 K to -1.39 eV at 2900 K at the fcc site. On the Al(111) surface, it changes from -3.35 eV at 0 K to -1.39 eV at 2900 K, indicating relatively stable adsorption across the temperature range on both surfaces.

For the oxygen molecule (O_2), the adsorption free energy decreases from -4.16 eV at 0 K to -1.61 eV at 2900 K on Cu(111). On Al(111), it decreases also, from -9.51 eV at 0 K to -6.72 eV. This shows a reduction in adsorption strength with temperature on both surfaces, more pronounced on Al(111).

The adsorption free energy of AlO becomes unlikely on the Cu(111) surface (0.67 eV) at 2900 K. On Al(111), adsorption decreases from -4.22 eV at 0 K to -1.55 eV at 2900 K. On Al(111), it decreases from -4.22 eV at 0 K to -1.55 eV at 2900 K. Similar behaviour is seen with either Al_2O or AlO_2 on Cu(111), with positive adsorption energies, 1.53 eV and 0.52 eV adsorption, respectively, at 2900 K, while on Al(111), it shifts from -2.26 eV at 0 K to 1.56 eV at 2900 K. On either surfaces, Al_2O adsorption becomes unlikely at 2900 K, with respectively 1.53 eV and 1.56 eV adsorption.

For AlO_2, the adsorption free energy is again positive (0.52 eV) at 2900 K on Cu(111). On Al(111), it decreases from -7.43 eV at 0 K to -3.61 eV at 2900 K. Lastly, Al_2O_2 shows endothermic budget for adsorption on either Cu(111) or Al(111) surfaces at 2900 K (1.85 eV and 0.63 eV, respectively).

When examining the behavior of different categories of species (oxygenated aluminates, oxygen species, and metallic species) as a function of temperature, distinct trends emerge. Oxygenated aluminates such as AlO, Al_2O, AlO_2, and Al_2O_2 tend to exhibit strong adsorption on Al(111) at lower temperatures, with a noticeable decrease in adsorption strength as temperature rises. This suggests that these species have a higher stability on Al(111) at low temperatures, but their interaction weakens at elevated temperatures. On Cu(111), these species generally show weaker adsorption energies, with AlO_2 being an exception due to its relatively stable adsorption across the temperature range.

Oxygen species like O and O_2 exhibit strong adsorption on both surfaces, particularly on Al(111), where O shows the highest adsorption energies at low temperatures. However, the adsorption energy decreases with

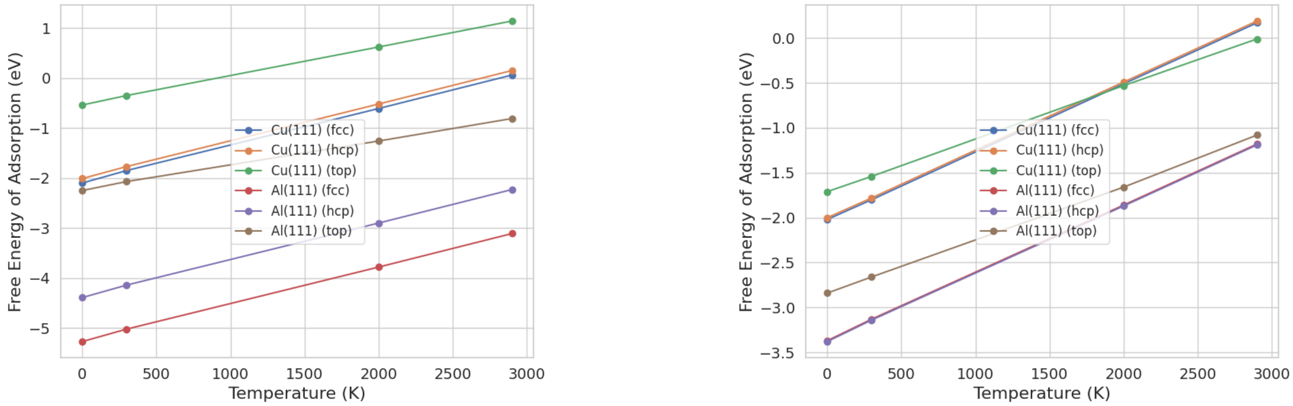

(a) Adsorption Free Energy of O on Cu(111) and Al(111).

(b) Adsorption Free Energy of Al on Cu(111) and Al(111).

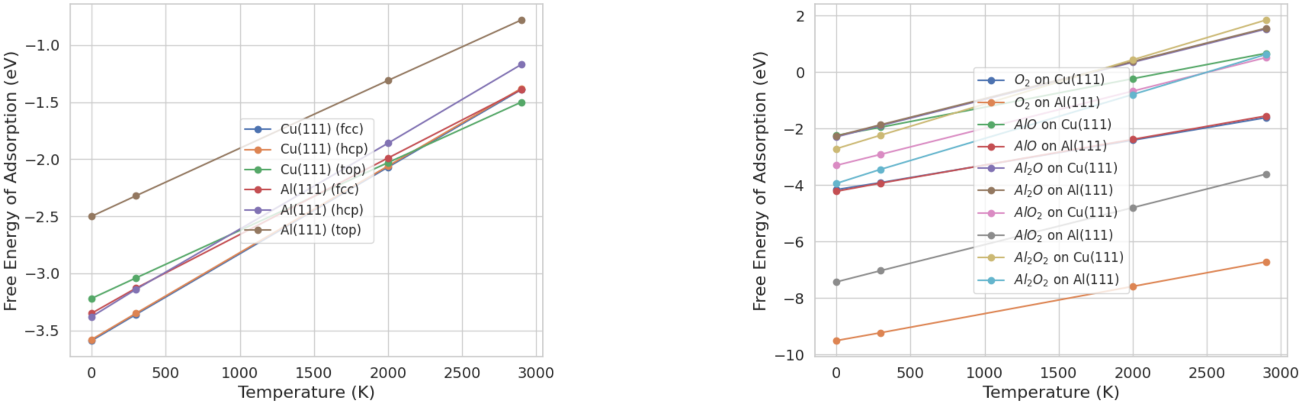

(c) Adsorption Free Energy of Cu on Cu(111) and Al(111).

(d) Adsorption Free Energy of Molecular Species on Cu(111) and Al(111).

FIG. 5: Comparison of adsorption free energies for different atomic and molecular species on Cu(111) and Al(111) at various temperatures.

increasing temperature, especially on Al(111), indicating a temperature-dependent weakening of the interaction. On Cu(111), the adsorption of O_2 remains strong even at higher temperatures, reflecting the reactivity of the surface towards oxygen molecules.

Metallic species, Al and Cu, display relatively stable adsorption energies on both surfaces, with a slight increase in adsorption strength at higher temperatures on Cu(111). On Al(111), the adsorption energies for Al decrease slightly with temperature, indicating weaker interaction at higher temperatures. The Cu(111) surface, being less reactive, shows consistently lower adsorption energies for these metals compared to Al(111), but the stability remains relatively unaffected by temperature changes. Overall, the temperature has a more pronounced effect on the adsorption of oxygenated aluminates and oxygen species, while metallic species exhibit more stable adsorption behavior.

In summary, combining the adsorption energy and free and free energy confirm that the Al(111) surface is highly reactive, leading to the spontaneous and strong adsorption of all the atoms and molecules considered in this work. In the case of molecules, this often results in their spontaneous dissociation and subsequent spatial separation due to hot adatom migration, aided by Coulombic repulsion, particularly between oxygen atoms. The adsorption energies on Al(111) generally range from approximately -4 to -5 eV, indicating strong interaction. On the other hand, the Cu(111) surface is found to be less reactive, with adsorption energies for atoms typically in the range of approximately -2 to -3 eV, roughly half of those on Al(111). Notably, barrierless dissociation was not observed on Cu(111) except for O_2, which still demonstrates some degree of reactivity. This behavior is illustrated in Figure 3, which compares the adsorption energies of the eight gaseous species (Al, Cu, O, O_2, Al_2O, Al_2O_2, AlO, and AlO_2) on both the Al and Cu surfaces. Given that aluminum is rarely entirely in its metallic state when exposed to air, particularly during thermite combustion, it is important to consider an oxidized aluminum surface, including both crystalline γ and amorphous Al_2O_3.

B. Comparative adsorption of *Cu*, *Al*, *O* atoms and O_2, *AlO*, Al_2O, AlO_2, Al_2O_2 molecules on γ and amorphous Al_2O_3 surfaces

The adsorption energies (ΔE_{ads}) of the different gaseous species onto γ-Al_2O_3 and amorphous Al_2O_3 (amAl_2O_3) are presented in Table VI. The Bader charge difference (ΔQ_{atomic}) upon adsorption of the different aluminum molecular suboxides are summarized in Table VII. Atomic distances for each stable configurations are reported in Table VIII. Note that in this subsection, we only report the most stable adsorbed configurations.

TABLE VI: Adsorption energies (ΔE_{ads} in eV) for the various gaseous species on amorphous and γ-Al_2O_3 surfaces. Only the most stable configuration is given for each atomic or molecular species.

	ΔE_{ads} (eV)	
Species	$\gamma Al_2O_3(100)$	amAl_2O_3
O	1.03	0.11
Al	-9.38	-4.46
Cu	-4.50	-2.81
O_2	-0.81	-0.67
AlO	-7.39	-7.11
Al_2O	-11.30	-15.05
AlO_2	-6.52	-5.17
Al_2O_2	-7.08	-5.45

Comparison of the amAl_2O_3, which provides a more realistic description of the viscous state of alumina at the high temperatures of thermite combustion (several thousands of K), is contrasted with its γ-Al_2O_3counterpart, which facilitates the stabilization of well-defined and categorized surface sites.

Starting with O, there is no possible adsorption, neither on γ-Al_2O_3, nor on the amorphous one. Adsorption energy is positive. Interestingly, O_2 molecule can adsorb onto both γ and amAl_2O_3 surfaces, but with a counter-intuitively low adsorption energy : $\Delta E_{ads} = \sim$ -0.81 eV and -0.67 eV, respectively. This suggests that, Al^{IV} and Al^{V} surface sites of the crystalline surface, and Al^{III}, Al^{IV}, and Al^{V} sites of the amorphous surface, cannot be modified by introducing additional oxygen atoms, unless pre-exposition to aluminum atoms to reduce the overall surface oxidation state strictly lower than Al^{III}.

By contrast, Al does adsorb on both alumina, with a highly stable configuration on the γ-Al_2O_3 with an energy gain of -9.38 eV. This high energy gain is due to the atomic insertion of the Al atom into the Al_2O_3 subsurface, allowing for the creation of up to five oxygen neighbours. In that configuration, the $Al_{\text{Sp}}-O_{\text{S}}$ and $Al_{\text{Sp}}-Al_{\text{S}}$ distances are of 1.72-1.84 Å and 2.58 Å, respectively. γ-Al_2O_3 features a stronger affinity and reactivity with Al atoms.

On the amAl_2O_3, Al_2O_3, the most energetically favorable configuration of Al stabilizes at -4.46 eV surrounded by 4 oxygen atoms with a cutoff equal to or below 2 Å.

Considering now Cu atoms, again, the most stable configuration is found on the γ-Al_2O_3 surface with an energy gain of -4.50 eV. The $Cu_{\text{Sp}}-O_{\text{S}}$ and $Cu_{\text{Sp}}-Al_{\text{S}}$ distances are of 1.87-2.11 Å and 2.87 Å, respectively. By contrast, on amAl_2O_3 surface, the most stable configuration stabilizes at -2.81 eV surrounded by 4 oxygen atoms with a cutoff equal to or below 2.2 Å.

TABLE VII: Bader charge difference (ΔQ_{atomic} in e) upon adsorption of different atoms from aluminum suboxide molecular species onto γ-Al_2O_3 surface. 'Sp' refers to as Species and 'S' refers to as the surface.

Species	ΔQ_{atomic} (e)			
	Al_{Sp}	O_{Sp}	Al_S	O_S
AlO	-1.23	0.40	-0.17	0.17−0.41
Al_2O	-1.59 & -1.61	-0.07	0.01−0.02	0.39−0.5
AlO_2	-0.29	0.50 & 0.47	-0.16 − -0.21	0.18
Al_2O_2	-0.04 & -1.48	-0.07 & 0.23	-0.12	0.3−20.49

Considering now the aluminum suboxide molecules, *AlO*, Al_2O, AlO_2, Al_2O_2, the most stable configurations and their respective adsorption energies on both surfaces are classified as follows:

1. Al_2O exhibits the most stable configuration with an adsorption energy of -11.30 eV. Interatomic distances are : $Al_{\text{Sp}} - O_{\text{S}}$: 1.76-1.85 Å, $Al_{\text{Sp}} - Al_{\text{S}}$: 2.67-3.00 Å, $Al_{\text{Sp}} - Al_{\text{Sp}}$: 2.86 Å) and $Al_{\text{Sp}} - O_{\text{Sp}}$: 1.75 & 1.78 Å. Bader charge differences indicate a significant contribution from aluminum (-1.59 − -1.61 e) during adsorption, which can also be seen in the electronic density difference ($\Delta\rho$) in Figure 6. This is in total agreement with the high reactivity of Al surface as more aluminum is incorporated into the surface more reactive is the surface. In the gaseous phase, AlO_2 adopts a configuration where the $O_{\text{Sp}} - Al_{\text{Sp}}$ bond distance measures 1.91 Å and both $\theta_{\text{Al-O-Al}}$ angles are equal to 120°. The $O_{\text{Sp}} - Al_{\text{Sp}}$ bond length is stretched upon adsorption and $\theta_{Al_{Sp}-O_{Sp}-Al_{Sp}}$ angles is 149°. After minimization, both Al_{Sp} are incorporated into the aluminum oxide network, turning themselves as Al^{III} and Al^{IV} surface sites.

2. *AlO* follows with an adsorption energy of -7.39 eV and interatomic distances being : $Al_{\text{Sp}} - O_{\text{S}}$: 1.78-2.49 Å, $O_{\text{Sp}} - Al_{\text{S}}$: 1.76 Å, $Al_{\text{Sp}} - Al_{\text{S}}$: 2.42 Å.

Again, Bader charge differences reveal a significant contribution from aluminum (-1.23 e) compared to oxygen (-0.4 e) as also seen in the electronic density difference ($\Delta\rho$) in Figure 6. In the gas phase, Al_2O_2 exhibits a configuration characterized by the $O_{\rm Sp} - Al_{\rm Sp}$ bond distance of 1.63 Å. Upon adsorption, it undergoes stretching without dissociation, with $O_{\rm Sp} - Al_{\rm Sp}$ distances of approximately 1.71 Å. The amount of energy (-7.39 eV) is due to the incorporation of the molecule as a coherent aluminum oxide surface site, increasing the number of Al-O bonds, as for Al_2O. Al_{Sp} becoming now a surface Al^{III} site.

3. Subsequently, Al_2O_2 exhibits an adsorption energy of -7.08 eV, with interatomic distances and Bader charge differences indicating significant contributions from both aluminum and oxygen. In the gas phase, Al_2O_2 showcases a configuration with a $O_{\rm Sp} - Al_{\rm Sp}$ bond distance of 1.77 Å and both $\theta_{\text{O-Al-S}}$ angles fixed at 93.5°. Upon adsorption, it undergoes a transformation without complete dissociation, featuring $O_{\rm Sp} - Al_{\rm Sp}$ distances and $\theta_{O_{Sp}-Al_{Sp}-S_{Sp}}$ angles spanning 66-127°. In this particular case while one Al is coherently incorporated, as for AlO, turning into a Al^{III} site, the second Al remains not fully incorporated, as a bridge surface site, which might be an explanation for not gaining as much energy as for AlO, pointing to the difficult molecular adaptation at 0 K on the alumina surface when bringing bigger molecules.

4. Finally, AlO_2 features an adsorption energy of -6.52 eV, accompanied by interatomic distances and Bader charge discrepancies indicating the involvement of both aluminum and oxygen during the adsorption process. In the gaseous phase, AlO_2 molecule adopts a configuration where the $O_{\rm Sp} - Al_{\rm Sp}$ bond distance measures 1.67 Å, and both $\theta_{O_{Sp}-Al_{Sp}-O_{Sp}}$ angles equal 180°. However, upon adsorption, it experiences deformation without dissociation, resulting in the stretching of $O_{\rm Sp} - Al_{\rm Sp}$ distances and bending of $\theta_{O_{Sp}-Al_{Sp}-O_{Sp}}$ angles at approximately 108°. However, the Al_{Sp} becomes now a surface Al^{III} site.

Importantly, the hierarchy is closely correlated to the amount of Al-O bond created upon adsorptions, and therefore, on the level of Al oxidation state. In this view, reaching Al^{IV} or Al^{V} states for incorporated Al_{Sp} guaranties the best adsorption level.

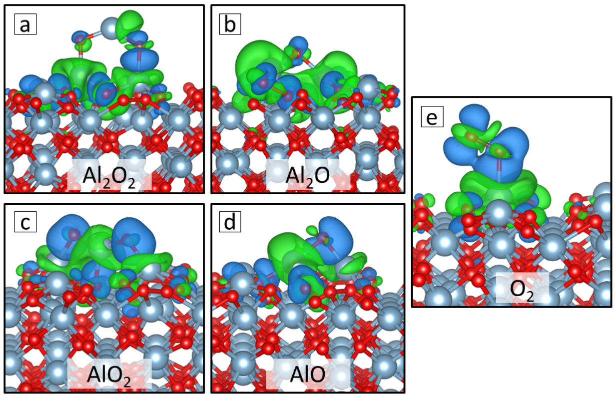

FIG. 6: (a–e) Electronic density ($\Delta\rho$) induced by the adsorption of aluminum suboxides (Al_2O_2, Al_2O, AlO_2, AlO, O_2) on γ-Al_2O_3 surface. The blue (green) zones indicate density increase (decrease). Steel blue balls represent Al atoms, and red balls represent O atoms.

Importantly results show that gaseous aluminum suboxides readily adsorb onto γ alumina surfaces with high energy gains. Instead of decomposing as seen on Al(111) surface, they insert adopting the $Al_2O_3(100)$ building block structures, and contribute the alumina growth. A parallel can be drawn with an epitaxial kind of growth process. This process is highly energetic (¿ -5 eV) and spontaneous. It is to be noted that the growth does not need any catalytic species nearby the adsorption site as proposed in earlier mechanistic approaches [38].

C. Discussing the $\mathbf{Al_2O_3}$ nucleation and growth on Cu, Al and $\mathbf{Al_2O_3}$

The thermokinetic models developped to describe Al/CuO thermite reactions [36–38] consider the condensation of Al_xO_y suboxides (x=1,2 and y=1,2) indifferently on the various Cu, Al, and Al_2O_3 surfaces. And, they conjecture that the condensation of Al_xO_y suboxides forms spontaneously stoichiometric Al_2O_3, either as a covering layer or as a cocluster growing appart from its pure metal host. Reactions are mostly written as the reaction of suboxide with gaseous O_2 or Al to form metastable Al_2O_3 that are subsequently adsorbed. In their study on Al particle combustion in air, Glorian *et al.* [74] introduced a DFT based condensation model of Al_xO_y suboxides on Al(111) surface, neglecting the potential nucleation and growth of Al_2O_3 byproducts, despite its crucial role in the aluminum reaction.

These new DFT results represent a significant advancement, not only complementing the existing kinetic data framework with quantified adsorption energies and dissociation paths on all condensed phases, including Cu, Al, and Al_2O_3, but also refining our understanding of the heterogeneous reactions involved in Al/CuO thermite combustion as it is discussed in the following.

Adsorptions of Al, Cu, O atoms and O_2, AlO, Al_2O,

TABLE VIII: Geometries (in Å and Deg) upon adsorption of different species onto $Al_2O_3(100)$ crystalline surface. 'Sp' refers to Species and 'S' refers to the surface.

Species	Distance Bond Lengths (Å)							
	$Al_{Sp} - O_S$	$O_{Sp} - Al_S$	$Al_{Sp} - Al_S$	$Cu_{Sp} - O_S$	$Cu_{Sp} - Al_S$	$Al_{Sp} - Al_{Sp}$	$Al_{Sp} - O_{Sp}$	$O_{Sp} - O_{Sp}$
O	−−	1.75	−−	−−	−−	−−	−−	−−
Al	1.72-1.84	−−	2.58	−−	−−	−−	−−	−−
Cu	−−	−−	−−	1.87-2.11	2.87	−−	−−	−−
O_2	−−	1.92	−−	−−	−−	−−	−−	1.29
AlO	1.78-2.49	1.76	2.42	−−	−−	1.71	−−	−−
Al_2O	1.76-1.85	−−	2.67-3.00	−−	−−	2.86	1.75-1.78	−−
AlO_2	1.80-1.81	1.80-1.82	3.00	−−	−−	−−	1.72-1.75	3.34
Al_2O_2	1.78-1.86	1.77-1.96	2.88-2.99	−−	−−	2.78	1.68-1.74	2.98

Species	Angles (°)	
	$\theta_{O_{Sp}-Al_{Sp}-O_{Sp}}$	$\theta_{Al_{Sp}-O_{Sp}-Al_{Sp}}$
Al_2O	−−	149
AlO_2	108	−−
Al_2O_2	65 & 126	108 & 121

AlO_2, Al_2O_2 molecules on Al and Al_2O_3 are spontaneous and highly exothermic on all surfaces, Cu, Al and Al_2O_3. However, significant differences were observed between the surfaces highlighting the manner in which alumina byproduct grows:

- *On the Al surface*, AlO, Al_2O, AlO_2, Al_2O_2 and O_2 molecules spontaneously dissociate and demonstrate spatial separation on the surface post-dissociation, facilitated by "hot adatom migration" assisted by the coulomb repulsion of oxygen adsorbates. We can conjecture a subsequent 2D-type of Al_2O_3 growth.

- *On the Cu surface*, although AlO, Al_2O, AlO_2, and Al_2O_2 molecules adsorb, they do not dissociate spontaneously. Note that O_2 dissociates but both atoms remain in close proximity on the surface, as opposed to its dissociation onto aluminum. We can speculate that the formation and growth of aluminum oxide on Cu will be localized, forming islands rather than a continuous layer as seen in byproducts analysed in previous studies [7].

- *On the Al_2O_3 surface (amorphous or γ)*, Al, AlO, Al_2O, AlO_2, and Al_2O_2 spontaneously adsorb, driving its growth through direct and non-dissociative incorporation of the basic suboxide units. In contrast, O and O_2 exhibit no reactivity on Al_2O_3 surfaces, when surface Al sites are in the Al^{III} or higher oxidation state. However, we anticipate that both O_2 and O, may contribute to the formation and growth of aluminum oxide layer after aluminum enrichment of the Al_2O_3 surface through adsorption of Al and Al_xO_y suboxides.

Explicit competition among these depicted mechanisms must be studied via molecular dynamics, which can explore the potential collective behavior and synergies of these processes. This is crucial for modeling how alumina byproduct grows from the early stage of its nucleation onto Al, Cu, and Al_2O_3 particles, and refining the Al vaporization process, which can be influenced by the growing alumina.

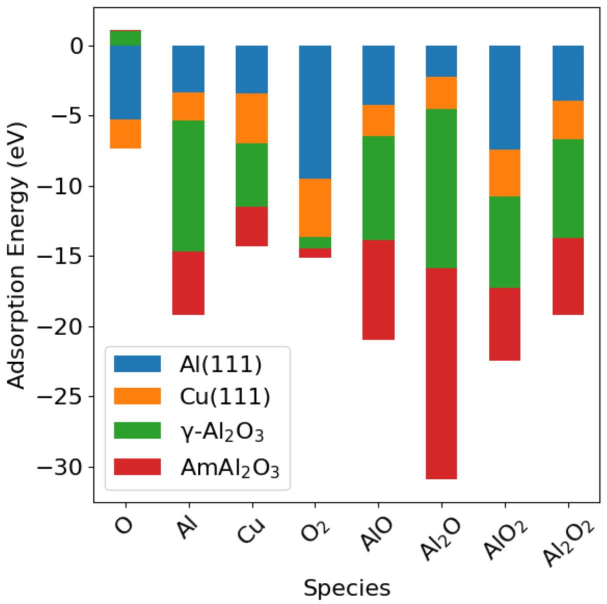

FIG. 7: Adsorption energies (ΔE_{ads} in eV) on Cu(111), Al(111), and Al_2O_3(100) surfaces, as well as amAl_2O_3 surface, for various species, including O, Al, and Cu atoms, O_2, AlO, Al_2O, AlO_2, and Al_2O_2 molecules. For the atomic species on Al(111) and Cu(111), only the most stable configurations are considered.

IV. CONCLUSION

This paper reports on a systematic investigation of the heterogeneous chemistry taking place during combustion of the Al/CuO thermite. The interactions of gas phase species, *e.g.*, Cu, Al, O atoms and O_2, AlO, Al_2O, AlO_2, Al_2O_2 molecules with Cu(111), Al(111), and Al_2O_3 surfaces are calculated using a DFT level of theory. Results point to the consistently higher reactivity of the Al(111) surface compared with Cu(111), notably showing barrierless dissociation and spatial spreading of the adsorbates with the help of the energy released by the chemical reaction and the effect of coulomb repulsion. This is believed to allow for a homogeneous 2D nucleation of the alumina upon reaction. In contrast, Cu(111) is roughly twice lower in reactivity compared with the Al(111) surface, showing non dissociative molecular states for all aluminum suboxides. The reduction of coulomb repulsion following O_2 dissociation is expected to allow for more localized nucleation of the aluminum oxide combustion product. The aluminum oxide surfaces exhibit strong reactivity with Al atoms and all Al suboxide species, which locally adapt their adsorbed configuration to enable the growth of stoichiometric alumina. Importantly, with surface aluminum atoms being in Al^{III} or more oxidation states, the alumina surface is not reactive to either O or O_2. These findings allows for a renewed understanding of the thermite thermochemistry, providing new mechanisms to distinguish Al from Cu condensed phases as well as for treating the specific alumina/gas phase interactions, which has been neglected to date. Such insights are pivotal to establishing a comprehensive thermokinetic database for the modelling of Al/CuO combustion, notably dealing with current effort at the level of fluid mechanics.

V. ACKNOWLEDGEMENT

The authors gratefully acknowledge the support received from the European Research Council (ERC, H2020 Excellent Science) Researcher Award (grant 832889-PyroSafe). Additionally, we would like to express our appreciation to the support received from the RHYO and Defi cle hydrogene vert from the Occitanie region. Finally we thank for the generous provision of high−power computing resources by CALMIP for conducting this research.

VI. COMPETING INTERESTS

The authors declare that there are no conflicts of interest, encompassing both personal relationships and financial factors, which could have influenced the publication of the study presented in this article.

VII. SUPPLEMENTAL MATERIAL

This section presents the Classical Molecular Dynamics simulation details for simulating the amorphous state of Al_2O_3, which is used in this work as the surface to be compared with the Al_2O_3(100) crystalline surface. This section also includes all POSCAR files for all the stable configurations presented in this study.

---

[1] M. Polis, A. Stolarczyk, K. Glosz, and T. Jarosz, Quo vadis, nanothermite? a review of recent progress, Materials **15**, 3215 (2022).
[2] E.-C. Koch and S. Knapp, Thermites–versatile materials, Propellants, Explosives, Pyrotechnics **44**, 7 (2019).
[3] K. S. Martirosyan, L. Wang, A. Vicent, and D. Luss, Nanoenergetic gas-generators: Design and performance, Propellants, Explosives, Pyrotechnics: An International Journal Dealing with Scientific and Technological Aspects of Energetic Materials **34**, 532 (2009).
[4] V. E. Sanders, B. W. Asay, T. J. Foley, B. C. Tappan, A. N. Pacheco, and S. F. Son, Reaction propagation of four nanoscale energetic composites (al/moo3, al/wo3, al/cuo, and b12o3), Journal of Propulsion and Power **23**,

707 (2007).

[5] D. Sundaram, V. Yang, and R. A. Yetter, Metal-based nanoenergetic materials: synthesis, properties, and applications, Progress in Energy and Combustion Science **61**, 293 (2017).

[6] R. Ramachandran, V. S. Vuppuluri, T. J. Fleck, J. F. Rhoads, I. E. Gunduz, and S. F. Son, Influence of stoichiometry on the thrust and heat deposition of on-chip nanothermites, Propellants, Explosives, Pyrotechnics **43**, 258 (2018).

[7] H. Wang, B. Julien, D. J. Kline, Z. Alibay, M. C. Rehwoldt, C. Rossi, and M. R. Zachariah, Probing the reaction zone of nanolaminates at s time and m spatial resolution, The Journal of Physical Chemistry C **124**, 13679 (2020).

[8] K. M. de Souza and M. J. S. de Lemos, Detailed numerical modeling and simulation of fe2o3- al thermite reaction, Propellants, Explosives, Pyrotechnics **46**, 806 (2021).

[9] S. F. Son, B. W. Asay, T. J. Foley, R. A. Yetter, M. H. Wu, and G. A. Risha, Combustion of nanoscale al/moo3 thermite in microchannels, Journal of Propulsion and Power **23**, 715 (2007).

[10] K. T. Sullivan, W.-A. Chiou, R. Fiore, and M. R. Zachariah, In situ microscopy of rapidly heated nano-al and nano-al/wo3 thermites, Applied Physics Letters **97** (2010).

[11] T. Wu, G. Lahiner, C. Tenailleau, B. Reig, T. Hungria, A. Esteve, and C. Rossi, Unexpected enhanced reactivity of aluminized nanothermites by accelerated aging, Chemical Engineering Journal **418**, 129432 (2021).

[12] F. Sevely, T. Wu, F. Sodre Ferreira, L. Seguier, V. Brossa, S. Charlot, A. Esteve, and C. Rossi, Developing a highly responsive miniaturized security device based on a printed copper ammine energetic composite, Sensors and Actuators A: Physical **346**, 113838 (2022).

[13] S. Pandey and C. Mastrangelo, Towards transient electronics through heat triggered shattering of off-the-shelf electronic chips, Micromachines **13**, 242 (2022).

[14] G. Taton, D. Lagrange, V. Conedera, L. Renaud, and C. Rossi, Journal of Micromechanics and Microengineering **23**, 105009 (2013).

[15] L. Glavier, A. Nicollet, F. Jouot, B. Martin, J. Barberon, L. Renaud, and C. Rossi, Nanothermite/rdx-based miniature device for impact ignition of high explosives, Propellants, Explosives, Pyrotechnics **42**, 308 (2017).

[16] C. Staley, C. Morris, R. Thiruvengadathan, S. Apperson, K. Gangopadhyay, and S. Gangopadhyay, Silicon-based bridge wire micro-chip initiators for bismuth oxide–aluminum nanothermite, Journal of Micromechanics and Microengineering **21**, 115015 (2011).

[17] Z. Yang, P. Zhu, Q.-y. Chu, Q. Zhang, K. Wang, H.-t. Jian, R.-q. Shen, Z. Yang, P. Zhu, Q.-y. Chu, Q. Zhang, K. Wang, H.-t. Jian, and R.-q. Shen, A micro-chip exploding foil initiator based on printed circuit board technology, Defence technology **18**, 1435 (2022).

[18] A. Nicollet, L. Salvagnac, V. Baijot, A. Estève, and C. Rossi, Sensors and Actuators A: Physical **273**, 249 (2018).

[19] T. Wu, F. Sevely, B. Julien, F. Sodre, J. Cure, C. Tenailleau, A. Esteve, and C. Rossi, New coordination complexes-based gas-generating energetic composites, Combustion and Flame **219**, 478 (2020).

[20] O. Odawara, T. Fujita, A. Gubarevich, and H. Wada, Thermite-related technologies for use in extreme geothermal environments, International Journal of Self-Propagating High-Temperature Synthesis **27**, 228 (2018).

[21] D. M. Dombroski, A. Wang, J. Z. Wen, and M. Alfano, Joining and welding with a nanothermite and exothermic bonding using reactive multi-nanolayers – a review, Journal of Manufacturing Processes **75**, 280 (2022).

[22] H. Jabraoui, M. D. Rouhani, C. Rossi, and A. Esteve, First-principles investigation of cuo decomposition and its transformation into cu 2 o, Physical Review Materials **6**, 096001 (2022).

[23] H. Jabraoui, A. Alpuche, C. Rossi, and A. Esteve, New insights into the mechanisms of tib2 (001) thermal oxidation combining molecular dynamics and density functional theory calculations, Acta Materialia **262**, 119463 (2024).

[24] H. Jabraoui, A. Esteve, M. Schoenitz, E. L. Dreizin, and C. Rossi, Atomic scale insights into the first reaction stages prior to al/cuo nanothermite ignition: influence of porosity, ACS applied materials & interfaces **14**, 29451 (2022).

[25] H. Jabraoui, A. Estève, S. Hong, and C. Rossi, Initial stage of titanium oxidation in ti/cuo thermites: a molecular dynamics study using reaxff forcefields, Physical Chemistry Chemical Physics **25**, 11268 (2023).

[26] T. Wu, V. Singh, B. Julien, C. Tenailleau, A. Estève, and C. Rossi, Pioneering insights into the superior performance of titanium as a fuel in energetic materials, Chemical Engineering Journal **453**, 139922 (2023).

[27] L. Marín, B. Warot-Fonrose, A. Estève, Y. J. Chabal, L. Alfredo Rodriguez, and C. Rossi, Self-organized al2cu nanocrystals at the interface of aluminum-based reactive nanolaminates to lower reaction onset temperature, ACS Applied Materials & Interfaces **8**, 13104 (2016).

[28] M. C. Rehwoldt, Y. Yang, H. Wang, S. Holdren, M. R. Zachariah, M. C. Rehwoldt, Y. Yang, H. Wang, S. Holdren, and M. R. Zachariah, Ignition of nanoscale titanium/potassium perchlorate pyrotechnic powder: Reaction mechanism study, Journal of physical chemistry. **122**, 10792 (2018).

[29] M. Mursalat, C. Huang, B. Julien, M. Schoenitz, A. Estève, C. Rossi, and E. L. Dreizin, Low-temperature exothermic reactions in al/cuo nanothermites producing copper nanodots and accelerating combustion, ACS Applied Nano Materials **4**, 3811 (2021).

[30] B. Julien, P. Dubreuil, C. Josse, L. Salvagnac, S. Pelloquin, A. Estève, and C. Rossi, Effect of substrate–induced localized stress on the combustion properties of al/cuo reactive multilayer films, Thin Solid Films **740**, 139000 (2021).

[31] A. Prakash, A. McCormick, and M. Zachariah, Tuning the reactivity of energetic nanoparticles by creation of a core- shell nanostructure, Nano Letters **5**, 1357 (2005).

[32] H. Wang, D. J. Kline, and M. R. Zachariah, In-operando high-speed microscopy and thermometry of reaction propagation and sintering in a nanocomposite, Nature communications **10**, 3032 (2019).

[33] K. Sullivan, N. Piekiel, C. Wu, S. Chowdhury, S. Kelly, T. Hufnagel, K. Fezzaa, and M. Zachariah, Reactive sintering: An important component in the combustion of nanocomposite thermites, Combustion and Flame **159**, 2 (2012).

[34] B. Julien, J. Cure, L. Salvagnac, C. Josse, A. Estève, and C. Rossi, Integration of gold nanoparticles to modulate the ignitability of nanothermite films, ACS Applied Nano Materials **3**, 2562 (2020).

[35] T. Wu, B. Julien, H. Wang, S. Pelloquin, A. Esteve, M. R. Zachariah, and C. Rossi, Engineered porosity-induced burn rate enhancement in dense al/cuo nanothermites, ACS Applied Energy Materials **5**, 3189 (2022).

[36] E. Tichtchenko, V. Folliet, O. Simonin, B. Bédat, L. Glavier, A. Esteve, and C. Rossi, Combustion model for thermite materials integrating explicit and coupled treatment of condensed and gas phase kinetics, Proceedings of the Combustion Institute **39**, 3637 (2023).

[37] E. Tichtchenko, B. Bédat, O. Simonin, L. Glavier, D. Gauchard, A. Esteve, and C. Rossi, Comprehending the influence of the particle size and stoichiometry on al/cuo thermite combustion in close bomb: A theoretical study, Propellants, Explosives, Pyrotechnics **48**, 202200334 (2023).

[38] V. Baijot, D.-R. Mehdi, C. Rossi, and A. Estève, A multi-phase micro-kinetic model for simulating aluminum based thermite reactions, Combustion and Flame **180**, 10 (2017).

[39] S. Kim, A. A. Johns, J. Z. Wen, and S. Deng, Burning structures and propagation mechanisms of nanothermites, Proceedings of the Combustion Institute **39**, 3593 (2023).

[40] G. Sun, J. Kürti, P. Rajczy, M. Kertesz, J. Hafner, and G. Kresse, Performance of the vienna ab initio simulation package (vasp) in chemical applications, Journal of Molecular Structure: THEOCHEM **624**, 37 (2003).

[41] G. Kresse and J. Hafner, Norm-conserving and ultrasoft pseudopotentials for first-row and transition elements, Journal of Physics: Condensed Matter **6**, 8245 (1994).

[42] P. E. Blöchl, O. Jepsen, and O. K. Andersen, Improved tetrahedron method for brillouin-zone integrations, Physical Review B **49**, 16223 (1994).

[43] H. Jabraoui, E. Hessou, S. Chibani, L. Cantrel, S. Lebègue, and M. Badawi, Adsorption of volatile organic and iodine compounds over silver-exchanged mordenites: A comparative periodic dft study for several silver loadings, Applied Surface Science **485**, 56 (2019).

[44] H. Jabraoui, D. Pech, M. D. Rouhani, C. Rossi, and A. Esteve, Insights into amorphous low-density hydrous ruo2 for supercapacitors using ab initio molecular dynamics simulations, Journal of Energy Storage **98**, 112926 (2024).

[45] S. Grimme, Semiempirical gga-type density functional constructed with a long-range dispersion correction, Journal of computational chemistry **27**, 1787 (2006).

[46] A. Benbella, H. Jabraoui, I. Matrane, and M. Mazroui, Exploring adsorption behavior of sulfur and nitrogen compounds on transition metal-doped cu (100) surfaces: insights from dft and md simulations, Physical Chemistry Chemical Physics **25**, 27553 (2023).

[47] H. Jabraoui, T. Charpentier, S. Gin, J.-M. Delaye, and R. Pollet, Atomic insights into the events governing the borosilicate glass–water interface, The Journal of Physical Chemistry C **125**, 7919 (2021).

[48] H. JABRAOUI, Thermodynamic corrections for adsorption energy calculated from static dft calculations, `https://github.com/JABRAOUI/Thermodynamic_corrections_adsorption_energy` (2024), accessed: 2024-08-09.

[49] Engineering toolbox (2001), `https://www.engineeringtoolbox.com/melting-boiling-temperatures-d_392.html`, accessed: 2001.

[50] C. T. Campbell and J. R. Sellers, The entropies of adsorbed molecules, Journal of the American Chemical Society **134**, 18109 (2012).

[51] M. W. Chase, Nist-janaf thermochemical tables 4th ed., J. of Physical and Chemical Reffernce Data , 1529 (1998).

[52] G. Henkelman, A. Arnaldsson, and H. Jónsson, A fast and robust algorithm for bader decomposition of charge density, Computational Materials Science **36**, 354 (2006).

[53] E. Sanville, S. D. Kenny, R. Smith, and G. Henkelman, Improved grid-based algorithm for bader charge allocation, Journal of computational chemistry **28**, 899 (2007).

[54] W. Tang, E. Sanville, and G. Henkelman, A grid-based bader analysis algorithm without lattice bias, Journal of Physics: Condensed Matter **21**, 084204 (2009).

[55] K. Momma and F. Izumi, Vesta: a three-dimensional visualization system for electronic and structural analysis, Journal of Applied crystallography **41**, 653 (2008).

[56] P. Abufager, P. Lustemberg, C. Crespos, and H. Busnengo, Dft study of dissociative adsorption of hydrogen sulfide on cu (111) and au (111), Langmuir **24**, 14022 (2008).

[57] C. Chang, C. Wei, and S. Chen, Self-diffusion of small clusters on fcc metal (111) surfaces, Physical review letters **85**, 1044 (2000).

[58] mp-776475: Al_2O_3 (Cubic, Ia3, 191). Materials Project, `https://next-gen.materialsproject.org/materials/mp-776475`, accessed on 2023-06-19.

[59] H. Jabraoui, S. Gin, T. Charpentier, R. Pollet, and J.-M. Delaye, Leaching and reactivity at the sodium aluminosilicate glass–water interface: Insights from a reaxff molecular dynamics study, The Journal of Physical Chemistry C **125**, 27170 (2021).

[60] H. Jabraoui, T. Charpentier, S. Gin, J.-M. Delaye, and R. Pollet, Behaviors of sodium and calcium ions at the borosilicate glass–water interface: Gaining new insights through an ab initio molecular dynamics study, The Journal of Chemical Physics **156** (2022).

[61] H. Jabraoui, S. Ouaskit, J. Richard, and J.-L. Garden, Determination of the entropy production during glass transition: Theory and experiment, Journal of Non-Crystalline Solids **533**, 119907 (2020).

[62] T. El Hafi, O. Bajjou, H. Jabraoui, J. Louafi, M. Mazroui, and Y. Lachtioui, Effects of cooling rate on the glass formation process and the microstructural evolution of silver mono-component metallic glass, Chemical Physics **569**, 111873 (2023).

[63] S. Assouli, H. Jabraoui, T. El hafi, O. Bajjou, A. Kotri, M. Mazroui, Y. Lachtioui, *et al.*, Exploring the impact of cooling rates and pressure on fragility and structural transformations in iron monatomic metallic glasses: Insights from molecular dynamics simulations, Journal of Non-Crystalline Solids **621**, 122623 (2023).

[64] S. Plimpton, Fast parallel algorithms for short-range molecular dynamics, Journal of computational physics **117**, 1 (1995).

[65] R. Dongol, L. Wang, A. Cormack, and S. Sundaram, Molecular dynamics simulation of sodium aluminosilicate glass structures and glass surface-water reactions using the reactive force field (reaxff), Applied Surface Science **439**, 1103 (2018).

[66] Y. Xu and M. Mavrikakis, Adsorption and dissociation of o2 on cu (111): thermochemistry, reaction barrier and the effect of strain, Surface science **494**, 131 (2001).

[67] M. Guiltat, M. Brut, S. Vizzini, and A. Hémeryck, Dioxygen molecule adsorption and oxygen atom diffusion on clean and defective aluminum (111) surface using first principles calculations, Surface Science **657**, 79 (2017).

[68] J.-X. Guo, L. Guan, F. Bian, Q.-X. Zhao, Y.-L. Wang, and B.-T. Liu, Oxygen adsorption on al (111) surface interstitial site calculated by density functional theory, Surface and interface analysis **43**, 940 (2011).

[69] E. Shustorovich and A. T. Bell, Oxygen-assisted cleavage of o h, n h, and c h bonds on transition metal surfaces: bond-order-conservation-morse-potential analysis, Surface science **268**, 397 (1992).

[70] C. M. Lousada and P. A. Korzhavyi, Oxygen adsorption onto pure and doped al surfaces–the role of surface dopants, Physical Chemistry Chemical Physics **17**, 1667 (2015).

[71] H. Brune, J. Wintterlin, R. Behm, and G. Ertl, Surface migration of “hot”adatoms in the course of dissociative chemisorption of oxygen on al (111), Physical review letters **68**, 624 (1992).

[72] E. F. Archibong and A. St-Amant, On the structure of al2o3 and photoelectron spectra of al2o2-and al2o3, The Journal of Physical ChemistryF A **103**, 1109 (1999).

[73] H. Jabraoui, M. Badawi, S. Lebègue, and Y. Vaills, Elastic and structural properties of low silica calcium aluminosilicate glasses from molecular dynamics simulations, Journal of Non-Crystalline Solids **499**, 142 (2018).

[74] J. Glorian, L. Catoire, S. Gallier, and N. Cesco, Gas-surface thermochemistry and kinetics for aluminum particle combustion, Proceedings of the Combustion Institute **35**, 2439 (2015).